
PERGAMON

Journal of the Mechanics and Physics of Solids
48 (2000) 867–897

JOURNAL OF THE
MECHANICS AND
PHYSICS OF SOLIDS

www.elsevier.com/locate/jmps

Crack channelling and spalling in a plate due to thermal shock loading

L.G. Zhao, T.J. Lu*, N.A. Fleck

Department of Engineering, University of Cambridge, Cambridge CB2 1PZ, UK

Received 12 May 1999; received in revised form 24 August 1999

Abstract

The propagation of a pre-existing edge crack across a finite plate subjected to cold shock has been studied. The plate, initially at uniform temperature, is exposed to a cold shock on one surface whilst three different types of heat transfer boundary condition are separately considered for the opposing face: cold shock, thermal insulation and fixed temperature. For all three boundary conditions, the plate experiences tensile stress near the cold-shocked surface and compressive stressing near the mid-plane. Consequently, a Mode I edge crack extending into the compressive region may grow in one of three different modes: continued extension in plane strain, channelling and spalling. The thermal shock conditions governing each failure mode are quantified, with a focus on crack channelling and spalling. The dislocation method is employed to calculate the energy release rates for plane strain cracking and steady-state channelling. For steady-state spalling, the energy release rate is obtained by an energy analysis of elastic beams far ahead and far behind the crack tip. Analytical solutions are also obtained in the short crack limit in which the problem is reduced to an edge crack extending in a half space; and the parameter range over which the short crack solution is valid for a finite plate is determined. Failure maps for the various cracking patterns are constructed in terms of the critical temperature jump and Biot number, and merit indices are identified for materials selection against failure by thermal shock.

Keywords: A. Crack branching; A. Fracture; B. Thermal stress; B. Crack mechanics

* Corresponding author. Tel.: +44-01223-766316; fax: +44-01223-332662.
E-mail address: tjl21@eng.cam.ac.uk (T.J. Lu).

0022-5096/00/$ - see front matter
PII: S0022-5096(99)00064-2

1. Introduction

In general, two alternative failure criteria can be used to determine the maximum jump in surface temperature that a material can sustain without cracking (i.e. its thermal shock resistance), one based on strength and the other based on fracture toughness (Hasselman, 1969; Nied, 1983; Rizk and Radwan, 1993; Jin and Mai, 1995; Lu and Fleck, 1998). The stress-based fracture parameter $\sigma_f/E\alpha$ is pertinent to the case of severe thermal shock of a solid containing small pre-existing cracks, and large values of the Biot number $Bi \equiv hH/k$. Here, σ_f, E, α and k are the tensile strength, elastic modulus, coefficient of thermal expansion and thermal conductivity of the material, H is a representative length scale (e.g. the sample thickness) and h is the surface heat transfer coefficient. The toughness-based fracture parameter for severe shock ($Bi \gg 1$) of a solid containing large pre-existing cracks is $K_{IC}/E\alpha$, where K_{IC} is the fracture toughness. Lu and Fleck (1998) explored both strength-controlled failure and toughness-controlled failure for the full range of Biot number Bi. At low Biot number, the resistance of a material to thermal shock is sensitive to its thermal conductivity, and the appropriate merit index for ranking material performance is $k\sigma_f/E\alpha$ for strength-controlled failure and $kK_{IC}/E\alpha$ for toughness-controlled failure. The transition flaw size a_T beyond which a toughness-based approach takes over from a strength-based approach is given by $a_T \approx (1/\pi)(K_{IC}/\sigma_f)^2$, as discussed by Lu and Fleck (1998).

Most previous studies on thermal shock failure are restricted to plane strain cracking. For a finite plate under cold shock, the usual problem under consideration is the propagation of a Mode I edge crack towards the centre of the plate. Two other failure modes, crack channelling and spalling, may nevertheless compete with plane strain cracking, as sketched in Fig. 1 for the case of a cold shock. The channelling and spalling of Mode I cracks under remote tensile loading have been analysed in detail by Hutchinson and Suo (1992). As the three-dimensional channelling crack extends, a steady state is achieved so that the crack

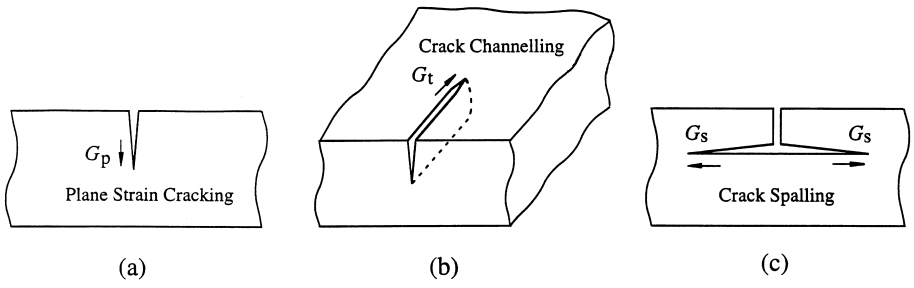

Fig. 1. Three different failure modes in cold shock: (a) plane strain cracking; (b) channelling; (c) spalling.

front shape remains constant. The steady-state energy release rate, G_t, averaged over the channelling crack front can be calculated directly from plane strain elasticity solutions. Based on this idea, Hutchinson and Suo (1992) and Beuth (1992) investigated the channelling of cracks through a thin film bonded to a substrate; in similar manner Ho and Suo (1993) and Chan et al. (1993) studied the tunnelling of cracks through constrained layers. Hitherto, crack channelling and spalling under transient thermal stressing have not been addressed.

1.1. Scope of the present study

In the current study, the propagation of a plane strain edge crack and the channelling and spalling of the crack within a finite plate are analysed in detail for the case of a cold shock. To cover a wide range of cold shock scenarios, three different heat transfer conditions are considered for the plate, held initially at uniform temperature T_i. In Case I, both the top and bottom surfaces of the plate are subjected to a cold shock with identical heat transfer coefficients. In Case II, the plate is subjected to a cold shock on the top surface, with perfect thermal insulation on the bottom face. In Case III, a cold shock is applied to the top surface of the plate while the bottom face is held at the initial temperature. For all three thermal boundary conditions the temperature and stress histories in the uncracked plate are obtained over the full range of Biot numbers. The surface subjected to a cold shock always experiences the highest tensile stress, and hence is the most likely site for the initiation of an edge crack. As discussed above, the crack may grow in one of three different modes: it may propagate in plane strain along the thickness direction of the plate (Fig. 1(a)), it may channel in the plane of the plate (Fig. 1(b)), or it may spall parallel to the surface of the plate (Fig. 1(c)). The energy release rate associated with a plane strain edge crack of arbitrary length is calculated as a function of time and Biot number, using the dislocation method. This result is subsequently used to compute the energy release rate associated with steady-state channelling. For steady-state spalling the energy release rate is calculated from the elastic energy stored in beams far ahead and far behind the crack tip, with the corresponding mode mix determined from the known solutions for a split beam (Hutchinson and Suo, 1992). An analytical solution is also obtained in the short crack limit by considering the propagation of an edge crack in a half-space. The range of validity of this solution is determined by direct comparison with the numerical results for an edge crack in a finite plate. Failure maps are constructed to display the thermal shock conditions governing plane strain cracking, crack channelling and spalling. Finally, merit indices for each mode of failure are obtained in order to aid the selection of engineering materials for thermal shock resistance.

2. Temperature and stress fields

2.1. The thermal model

Consider an infinitely large plate of thickness $2H$ and uniform initial temperature T_i, and let Cartesian co-ordinates (x, z) be embedded at the centre of the plate, as depicted in Fig. 2. At time $t = 0$, the plate is suddenly exposed at its top surface ($z = H$) to a convective cooling medium of temperature T_∞ such that

$$k\frac{\partial T(z, t)}{\partial z} = -h(T - T_\infty), \quad \text{at } z = H \tag{1}$$

where k is the thermal conductivity of the material from which the plate is made, h is the coefficient of heat transfer, and $T(z, t)$ is the temperature distribution of the plate. At the bottom surface ($z = -H$), one of the following three different heat transfer boundary conditions is assumed to hold, see Fig. 2.

Case I is an identical cold shock to the top surface, with

$$k\frac{\partial T(z, t)}{\partial z} = h(T - T_\infty), \quad \text{at } z = -H \tag{2a}$$

Case II is thermal insulation, with

$$\frac{\partial T(z, t)}{\partial z} = 0, \quad \text{at } z = -H \tag{2b}$$

and Case III is a constant temperature equal to the initial temperature,

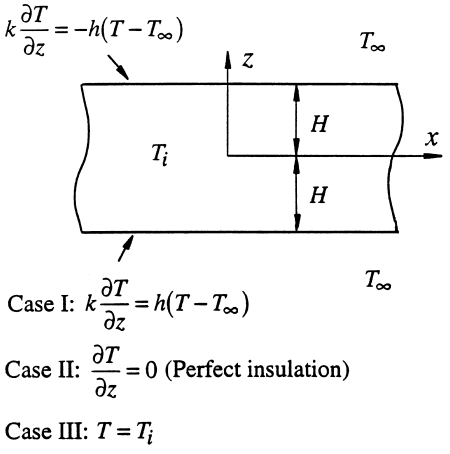

Fig. 2. A crack-free plate of thickness $2H$ subjected to three different types of cold shock where $T_i > T_\infty$.

$$T = T_i, \quad \text{at } z = -H \tag{2c}$$

The transient temperature distribution in the plate is governed by the Fourier law of conduction

$$\frac{\partial^2 T(z,\, t)}{\partial z^2} = \frac{1}{\kappa}\,\frac{\partial T(z,\, t)}{\partial t}, \qquad |\, z\,| \le H \tag{3}$$

where κ is the thermal diffusivity of the material. For simplicity, the material is assumed to be isotropic, with thermo-physical properties independent of temperature; the results obtained in the following sections can be extended to orthotropic materials by using the technique of orthotropic scaling (Hutchinson and Suo, 1992; Lu and Fleck, 1998).

2.2. Evolution of temperature and stress

Eq. (3) and the associated initial and boundary conditions can be solved by the standard separation-of-variables technique (Carslaw and Jaeger, 1959). For Case I, the non-dimensional temperature field is found to be

$$\bar{T}(z,\, t) \equiv \frac{T(z,\, t) - T_i}{T_i - T_\infty} = -1 + 2\sum_{n=1}^{\infty} \frac{\sin\beta_n \cos(\beta_n z/H)}{\beta_n + \sin\beta_n \cos\beta_n} \exp\left(-\beta_n^2 \frac{\kappa t}{H^2} \right) \tag{4}$$

where β_n are the positive roots of $\beta \tan\beta = Bi$; the corresponding solutions for Cases II and III are given in Appendix A [cf Eqs. (A1) and (A3)]. The evolution of temperature in the uncracked plate under cold shock ($T_i > T_\infty$), as predicted separately from Eqs. (4), (A1) and (A3), is plotted in Fig. 3 for selected values of dimensionless time $\bar{t} \equiv \kappa t/H^2$. Here, for brevity, results are presented only for the case of $Bi = 10$, which is typical for the quenching of glass in ice water; results over the full range of Biot number ($0 < Bi < \infty$) are qualitatively similar to those shown in Fig. 3. It is interesting to note from Figs. 3(a) and (b) that Cases II and III give almost the same temperature distribution in the upper half of the plate ($\bar{z} > 0$) during the initial stage of cold shock ($\bar{t} < 0.4$). This is because, in Cases II and III, the time for the 'thermal front' to traverse the plate is $\bar{t} \cong 0.4$ (Lu and Chen, 1999).

Once the temperature field has been determined, it is relatively straightforward to determine the transient thermal stress distribution in the plate from considerations of force and moment equilibrium. It is assumed that the plate is free to expand with vanishing in-plane force resultants

$$\int_{-H}^{H} \sigma_{xx}(z,\, t)\mathrm{d}z = 0, \qquad \int_{-H}^{H} \sigma_{yy}(z,\, t)\mathrm{d}z = 0 \tag{5}$$

and vanishing normal stress in the through-thickness direction, $\sigma_{zz} = 0$. In addition equilibrium dictates that the bending moment due to the thermal stresses vanishes, giving

$$\int_{-H}^{H} \sigma_{xx}(z, t) z \, \mathrm{d}z = 0 \quad \text{and} \quad \int_{-H}^{H} \sigma_{yy}(z, t) z \, \mathrm{d}z = 0 \tag{6}$$

Note that the temperature distribution is unsymmetrical about the mid-plane $z = 0$ in Cases II and III, resulting in a finite plate curvature. It follows from Eqs. (5) and (6) that the transient stress $\sigma_{xx}(z, t)$ induced by the temperature distribution $T(z, t)$ can be written in the following non-dimensional form (cf Manson, 1966)

$$\bar{\sigma}(z, t) \equiv \frac{\sigma_{xx}(z, t)}{\bar{E}\bar{\alpha}(T_{\mathrm{i}} - T_{\infty})} = -\frac{T - T_{\mathrm{i}}}{T_{\mathrm{i}} - T_{\infty}} + \frac{1}{2H}\int_{-H}^{H} \frac{T - T_{\mathrm{i}}}{T_{\mathrm{i}} - T_{\infty}} \mathrm{d}z + \frac{3z}{2H^3}\int_{-H}^{H} \frac{T - T_{\mathrm{i}}}{T_{\mathrm{i}} - T_{\infty}} z \, \mathrm{d}z \tag{7}$$

where $\bar{E} = E/(1-\nu^2)$ and $\bar{\alpha} = \alpha(1+\nu)$. Here, E, ν and α denote Young's modulus, Poisson's ratio, and the coefficient of thermal expansion, respectively. For Case I, substitution of (4) into (7) leads to

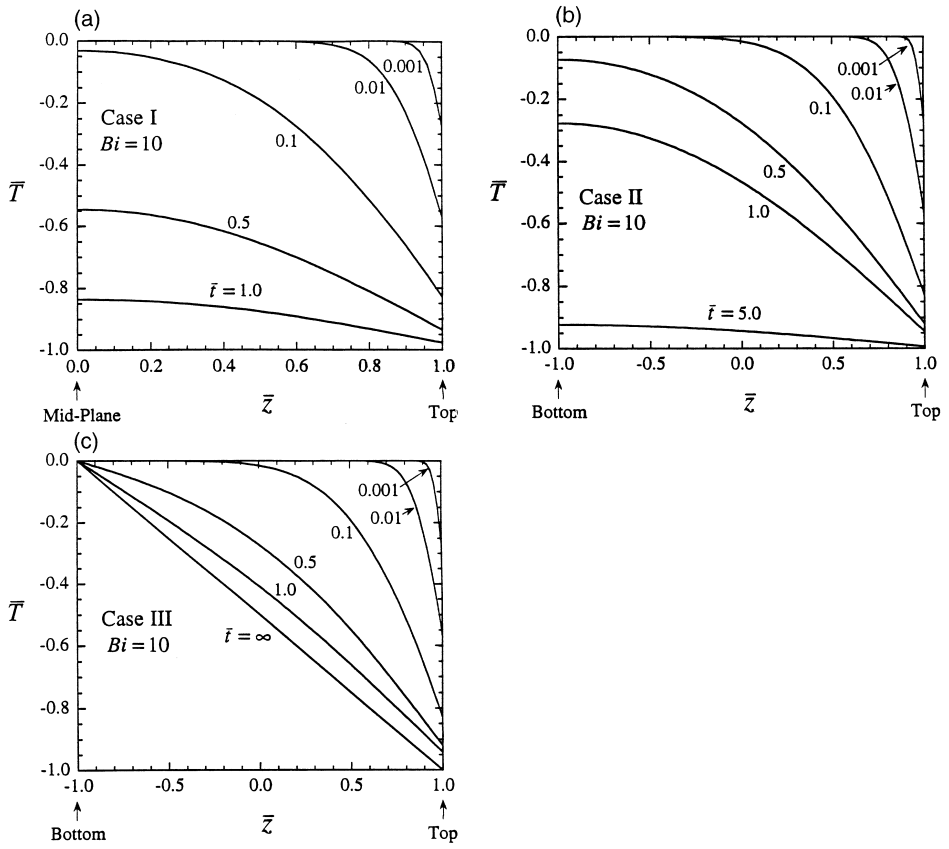

Fig. 3. Transient temperature distribution in the plate under cold shock with Biot number $Bi = 10$: (a) Case I; (b) Case II; (c) Case III.

$$\bar{\sigma}(z,\,t) = -2\sum_{n=1}^{\infty}\frac{\sin\ \beta_n}{\beta_n + \sin\ \beta_n\ \cos\ \beta_n}\left\{\cos\left(\beta_n\frac{z}{H}\right) - \frac{\sin\ \beta_n}{\beta_n}\right\}\exp\left(-\beta_n^2\frac{\kappa t}{H^2}\right) \tag{8}$$

For brevity, the stress fields in the plate corresponding to Cases II and III boundary conditions are presented in Appendix A.

Recall that in the limiting case of a thermally insulated plate ($Bi = 0$) the plate is everywhere stress-free, whereas it suffers the most stringent thermal stressing when $Bi \to \infty$. The normalised stress $\bar{\sigma}(z,\,t) = \sigma(z,\,t)/\bar{E}\bar{\alpha}(T_i - T_\infty)$ is plotted in Fig. 4 for the choice of Biot number $Bi = 10$ and for selected values of dimensionless time $\bar{t} = \kappa t/H^2$. At any given instant, the top surface of the plate experiences the largest tensile stress, and is expected to be the site of crack initiation. For Case I, symmetry dictates that both the top and bottom surfaces experience the same tensile stress history, implying that edge cracks may initiate

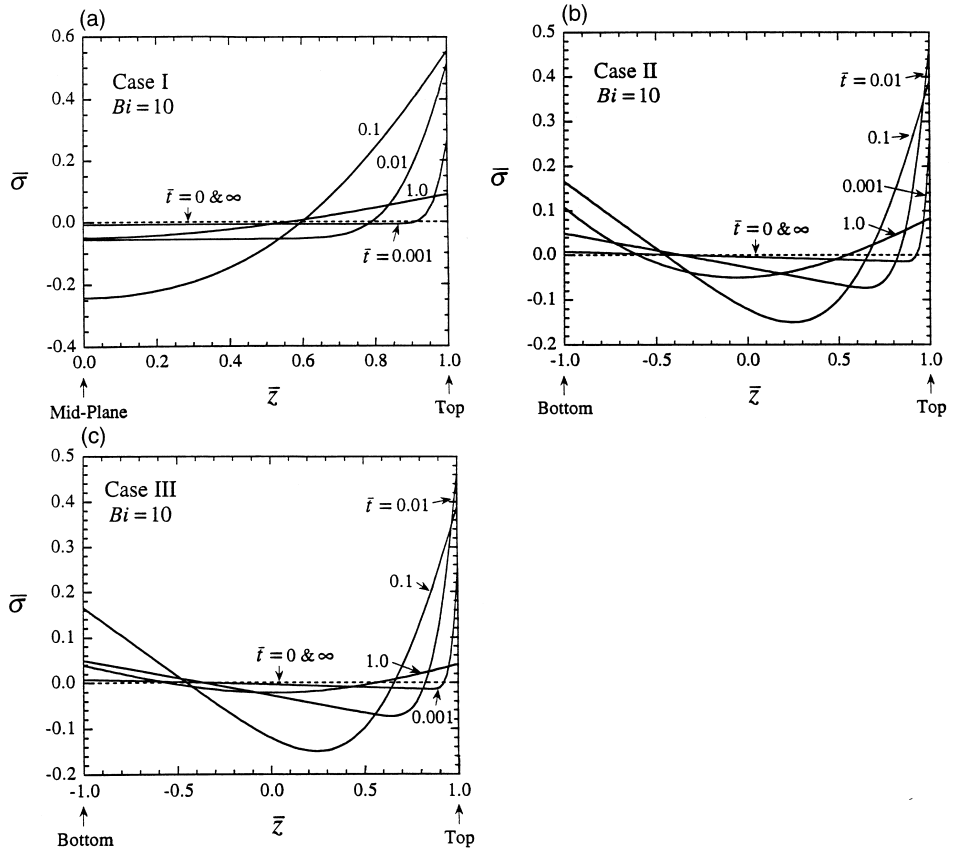

Fig. 4. Transient stress distribution in the plate under cold shock with Biot number $Bi = 10$: (a) Case I; (b) Case II; (c) Case III.

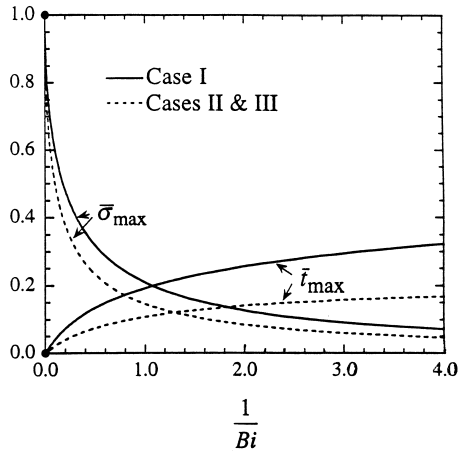

Fig. 5. Maximum tensile stress, $\bar{\sigma}_{max}$, at the top surface of the strip and the corresponding time elapse, $\bar{t}_{max}$, plotted as a function of Biot number Bi.

from either surface. It is known from a comparison of the stress intensity factor solutions for a single edge crack, and for two opposing edge cracks of equal length that the initiation of a single edge crack is energetically more favourable than the initiation of two symmetrical edge cracks (Hutchinson and Suo, 1992); hence, the propagation of a single edge crack will be the focus of our study. It is also noted that, in the early stages of a cold shock ($\bar{t} < 0.4$), almost identical stress fields are generated in Cases II and III in the region $\bar{z} > 0$ as a direct consequence of the nearly identical temperature distributions [recall Figs. 3(b) and (c)].

For all three cases considered, the maximum tensile stress $\bar{\sigma}_{max}$ attained at the top surface of the plate together with its time of occurrence $\bar{t}_{max}$ are plotted against $1/Bi$ in Fig. 5. The values for $\bar{\sigma}_{max}$ and $\bar{t}_{max}$ in Cases II and III are nearly identical. The following approximations for $\bar{\sigma}_{max}$ and $\bar{t}_{max}$ have the correct asymptotic behaviours and are found to describe closely the computed values shown in Fig. 5,

$$\bar{\sigma}_{max}(0, t_{max}) = \left\{1.5 + \frac{3.25}{Bi} - 0.5\, e^{-16/Bi}\right\}^{-1}, \quad \bar{t}_{max} = \frac{0.42}{1 + 1.18\, Bi} \tag{9a}$$

for Case I and

$$\bar{\sigma}_{max}(0, t_{max}) = \left\{1.5 + \frac{5.55}{Bi} - 0.5\, e^{-44/Bi}\right\}^{-1}, \quad \bar{t}_{max} = \frac{0.21}{1 + 0.88\, Bi} \tag{9b}$$

for Cases II and III. Similar curve-fitting formulae have been proposed by Manson (1966). It is clear that the magnitude of $\bar{\sigma}_{max}$ increases with increasing Biot number Bi; in the limit $Bi \to \infty$, we find that $\bar{\sigma}_{max} = 1$ and $\bar{t}_{max} = 0$. Of the

three cases studied, the constraint imposed by the Case I boundary condition produces the largest $\bar{\sigma}_{\max}$ — although the corresponding time of occurrence $\bar{t}_{\max}$ is also the longest.

3. Plane strain cracking under thermal shock

The results presented above indicate that, under cold shock, cracks are most likely to initiate from the top surface of the plate. Once such an edge crack has formed, it may grow in one of three different modes as sketched in Fig. 1. We begin the crack analysis by considering the idealised case of an isolated Mode I edge crack of depth a (Fig. 6(a)). The analysis presented here builds upon that given already by Lu and Fleck (1998) for an edge crack under Case I boundary conditions. It is assumed that the plate contains a distribution of flaws on the scale of the structural dimension, and that the crack commences from the "worst flaw" having the largest driving force, i.e., the greatest energy release rate. In this section, plane strain cracking is analysed to provide baseline solutions for channelling (Section 4) and spalling (Section 5); results for the short crack limit of an edge crack in a half space are presented in Section 6. For plane strain cracking, channelling and spalling in a finite plate, emphasis is placed on finding the energy release rate maximised with respect to crack length and time as a function of the Biot number. As will become evident later, these solutions are no longer valid as the plate thickness $2H \to \infty$ (i.e. $Bi \to \infty$); short crack solutions must then be used.

For an edge crack propagating in plane strain (Fig. 1(a)), the energy release rate

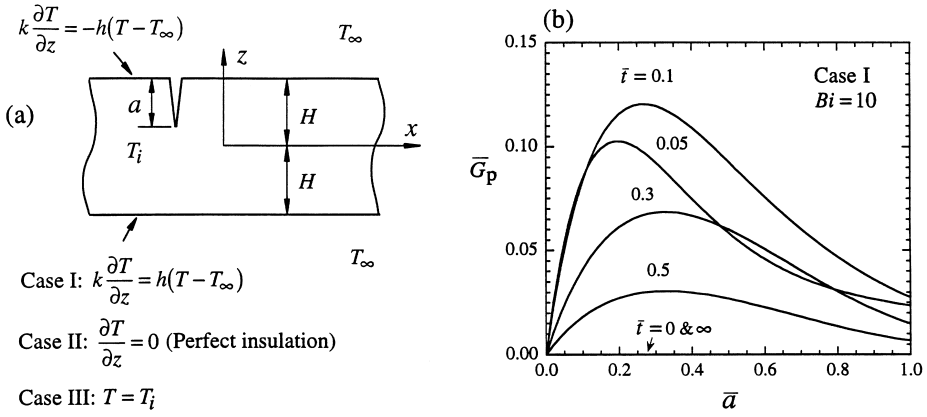

Fig. 6. (a) An infinite plate embedded with a pre-existent crack subjected to three different types of cold shock, and (b) energy release rate G_p as a function of crack size and elapsed time for plane strain cracking (Case I with $Bi = 10$).

G_p at the crack tip is given by

$$G_p = \frac{K_I^2}{\bar{E}} \tag{10}$$

where the Mode I stress intensity factor K_I can be determined by the dislocation method. Here the Mode I edge crack is modelled as a continuous distribution of edge dislocations. The crack face traction boundary condition is enforced by integrating the traction contribution on the crack face ($x = 0$) due to the distribution of dislocations, resulting in the singular integral equation,

$$\int_0^a \frac{2A(s)}{z-s}\mathrm{d}s + \int_0^a A(s)H(s, z)\mathrm{d}s = -\sigma(z, t), \quad 0 < z < a \tag{11}$$

where $\sigma(z, t)$ is the thermal stress distribution along the crack line, $A(s)$ is the density of edge dislocations, and the kernel function $H(s, z)$ is given by Civelek (1985). Following Erdogan et al. (1973), the dislocation density function $A(s)$ is expanded as a series of Jacobi polynomials $P_{k-1}^{(-1/2,\ 1/2)}(\xi)$, such that

$$A(s) = A(\xi) = \sqrt{\frac{1+\xi}{1-\xi}} \sum_{k=1}^{N} C_k P_{k-1}^{(-1/2,\ 1/2)}(\xi) \tag{12}$$

upon making use of the changes of variables

$$s = \frac{(1+\xi)}{2}a, \quad -1 < \xi < 1 \tag{13}$$

By selecting N collocation points on the crack surface to match the boundary condition (11), a system of linear equations is obtained to determine the coefficients C_k for k in the range 1 to N. Once the solution has been obtained, the stress intensity factor K_I and the opening displacement $\delta(a')$ at any point a' on the crack face are calculated from the expressions

$$K_I = 2\pi\sqrt{\pi a} \sum_{k=1}^{N} C_k P_{k-1}^{(-1/2,\ 1/2)}(1) \tag{14}$$

and

$$\delta(a') = \int_{a'}^{a} A(s)\mathrm{d}s$$

For the Case I temperature boundary condition with $Bi = 10$, the normalised energy release rate $\bar{G}_p \equiv G_p/\bar{E}\bar{\alpha}^2 H(T_i - T_\infty)^2$ predicted by the dislocation method is plotted in Fig. 6(b) against dimensionless crack lengths $\bar{a} \equiv a/H$, for selected values of dimensionless time $\bar{t} \equiv \kappa t/H^2$. As a check, we have solved the same problem by using the weight function method (Tada et al., 1985; Lu and Fleck, 1998). The predictions are in close agreement with those obtained from the

dislocation method — the latter method is more accurate but is computationally more intensive. In the remainder of this paper, unless otherwise stated, all calculations have been performed by the dislocation method. We note that $\bar{G}_p$ attains a peak value for all values of crack length at $\bar{t} \approx 0.1$; the global maximum of $\bar{G}_p$ is attained at $\bar{t} \approx 0.1$ and $\bar{a} \approx 0.25$. For Cases II and III and for Biot numbers over the full range $0 < Bi < \infty$, the results are qualitatively similar to those shown in Fig. 6(b) for Case I.

Consider the case of a pre-existing plane strain edge crack of length a in a plate with a given Biot number Bi; then G_p attains its peak value $(G_p)_{peak}$ after a time t_{peak}. When $(G_p)_{peak}$ equals the toughness G_{IC}, plane strain cracking occurs; otherwise, the edge crack either arrests or advances in other modes such as

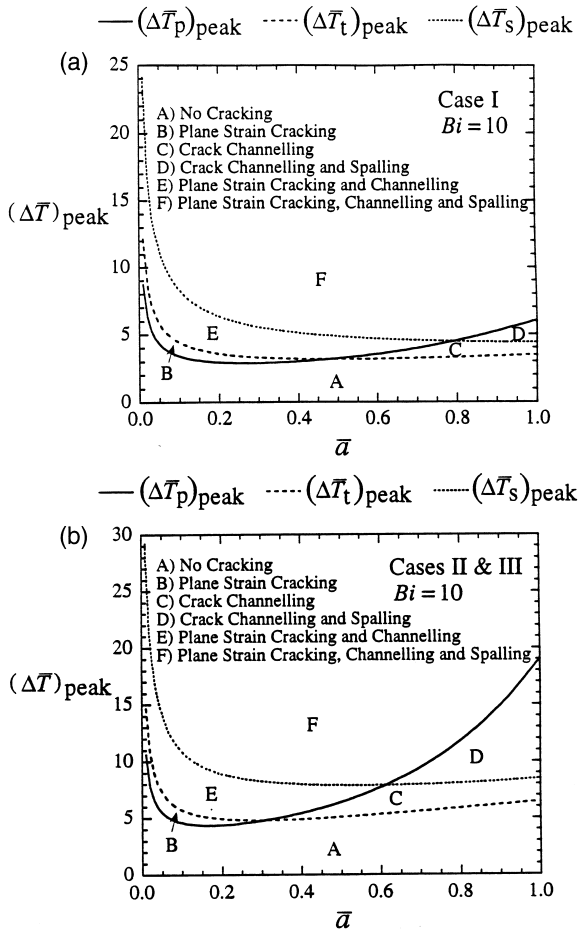

Fig. 7. Failure map for plane strain cracking, channelling and spalling, with $Bi = 10$. (a) Case I; (b) Cases II and III ($Bi = 10$).

channelling and spalling. On recalling the connection $G \propto (\Delta T)^2$ where $\Delta T \equiv T_i - T_\infty$ is the temperature jump at the top surface of the plate, the fracture criterion $(G_p)_{peak} = G_{IC}$ can be used to evaluate the critical surface temperature jump $(\Delta T_p)_{peak}$ to cause plane strain cracking as a function of a and Bi. For illustration, Fig. 7(a) plots the predicted $(\Delta \bar{T}_p)_{peak} \equiv (\Delta T_p)_{peak}/\sqrt{G_{IC}/(\bar{E}\bar{\alpha}^2 H)}$ against the dimensionless crack size $\bar{a} = a/H$ for $Bi = 10$ and Case I boundary condition. We emphasise that $(\Delta T_p)_{peak}$ is the maximum temperature jump that can be applied to the plate without causing plane strain cracking, over all time, for any fixed crack length and Biot number. Similar calculations are reported below for steady-state channelling and spalling, and the corresponding critical temperature jumps are included in Fig. 7(a) as dashed lines (channelling) and dotted lines (spalling). For Cases II and III, the results are summarised in Fig. 7(b), where again a value $Bi = 10$ is assumed.

Fig. 7 can be used as a failure map to determine which one of the failure modes is most likely to occur when a material embedded with a pre-existent flaw is subjected to cold shock. Depending upon the size of the flaw, this may happen in one of the six crack patterns indicated in Fig. 7: (A) no cracking; (B) plane strain cracking; (C) channelling; (D) channelling and spalling; (E) plane strain cracking and channelling; (F) plane strain cracking, channelling and spalling. Note that, in general, plane strain cracking tends to dominate when the flaw size a is small, whereas channelling and/or spalling is preferred when a is large.

For a given Biot number Bi, $G_p(t, a)$ achieves a global maximum value $(G_p)_{max}$ after a time t_c and for a particular crack length a_c. Non-dimensional values of $(G_p)_{max}$ have been obtained as functions of Bi for the three boundary conditions, Cases I–III. It is found that the following simple curve-fitting formulas are in good agreement with the numerical values

$$(\bar{G}_p)_{max} \equiv \frac{(G_p)_{max}}{G_0} = 0.187\left(1 + \frac{2.2}{Bi}\right)^{-2}, \quad \text{Case I} \tag{16}$$

$$(\bar{G}_p)_{max} \equiv \frac{(G_p)_{max}}{G_0} = 0.098\left(1 + \frac{2.9}{Bi}\right)^{-2}, \quad \text{Cases II and III} \tag{17}$$

where $G_0 = \bar{E}\bar{\alpha}^2 H(T_i - T_\infty)^2$. We note that the limiting value of the energy release rate for Case I is $(G_p)_{max} = 0.187\bar{E}\bar{\alpha}^2 H(T_i - T_\infty)^2$ at $a/H \approx 1/4$ and $\kappa t/H^2 = 0.06$. This energy release rate, attained under the most severe thermal shock boundary condition $Bi = \infty$, exceeds the largest values obtained for Cases II and III. A comparison with the energy release rates obtained below for channelling and spalling also reveals that this value of $(G_p)_{max}$ is the highest achieved for the three cracking modes under any boundary condition considered. However, we emphasise that the limit $Bi = \infty$, when applied to Eqs. (16) and (17), should be interpreted as $h \to \infty$ at finite H and not $H \to \infty$ at finite h, i.e., Eqs. (16) and (17) do not apply in the latter case. The limiting case of an edge crack extending in a semi-infinite solid (i.e., $H \to \infty$) will be discussed later in Section 6.

On recalling that $\bar{G}_p \equiv G_p/\bar{E}\bar{\alpha}^2(T_i - T_\infty)^2$, Eqs. (16) and (17) can be used together with the fracture criterion, $(G_p)_{max} = G_{IC}(\equiv K_{IC}^2/\bar{E})$ to determine the maximum surface temperature jump that can be applied to the plate without incurring plane strain cracking, $(\Delta T_p)_{max}$, as a function of the Biot number *Bi*. The resulting dimensionless maximum temperature jump $(\Delta\bar{T}_p)_{max} \equiv (\Delta T_p)_{max}\,\bar{\alpha}\sqrt{\bar{E}H}/\sqrt{G_{IC}}$ and the corresponding values of $\bar{t}_c \equiv \kappa t_c/H^2$ and $\bar{a}_c \equiv a_c/H$ at which $(\Delta\bar{T}_p)_{max}$ occurs are plotted in Fig. 8 as a function of *Bi* for Cases I–III. Curve-fitting formulae for these results are

$$(\Delta\bar{T}_p)_{max} \equiv (\Delta T_p)_{max}\,\frac{\bar{E}\bar{\alpha}\sqrt{H}}{K_{IC}} = 2.31 + \frac{5.05}{Bi} \tag{18a}$$

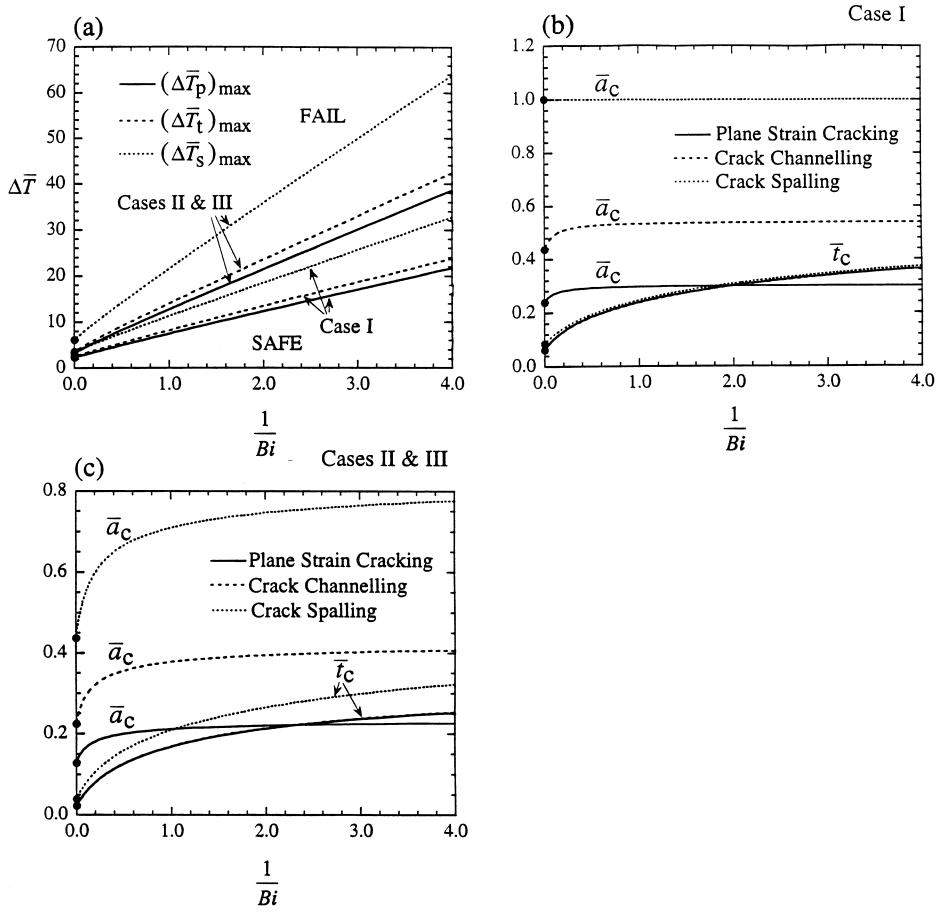

Fig. 8. (a) Maximum surface temperature jump (thermal shock resistance) as a function of a Biot number for all three cases. Critical crack size and time elapse for (b) Case I and (c) Cases II and III.

$$\bar{t}_c \equiv \frac{\kappa t_c}{H^2} = 0.06 + \frac{0.43}{1 + 1.5\ Bi} \tag{18b}$$

$$\bar{a}_c \equiv \frac{a_c}{H} \approx 0.3 \tag{18c}$$

for Case I, and

$$(\Delta \bar{T}_p)_{max} \equiv (\Delta T_p)_{max} \frac{\bar{E}\bar{\alpha}\sqrt{H}}{K_{IC}} = 3.18 + \frac{9.2}{Bi} \tag{19a}$$

$$\bar{t}_c \equiv \frac{\kappa t_c}{H^2} = 0.02 + \frac{0.3}{1 + Bi} \tag{19b}$$

$$\bar{a}_c \equiv \frac{a_c}{H} \approx 0.22 \tag{19c}$$

for Cases II and II. We note in passing that Eqs. (18a) and (b) are slightly more accurate than the previous curve fitting results of Lu and Fleck (1998).

4. Channelling under thermal shock

Consider the propagation of a plane strain edge crack in a plate under cold shock. For all three boundary conditions considered (Fig. 6(a)) we predict that the plane strain crack propagates unstably at short crack lengths, whereas for long cracks the energy release rate decreases with increasing a. This decreasing driving force is due to the presence of compressive stress in the central portion of the plate. In addition to advance in the through-thickness direction, a crack can advance in other modes, such as by channelling or spalling.

The channelling of an edge crack is a complicated, three-dimensional process difficult to analyse. However, for a sufficiently long channelling crack, a steady state is reached whereby the crack channels at fixed depth, with a constant tip shape and constant energy release rate. The steady-state energy release rate, G_t, averaged over the depth of the channelling crack front can be directly calculated from the plane strain elasticity solutions presented in the previous section. If it is assumed that the toughness of the solid G_{IC} is independent of the mode mix around the periphery of the curved crack front then a fracture criterion for channelling can be written as $G_t = G_{IC}$. Considerations of energy balance lead to two alternative but equivalent formulas for G_t (Hutchinson and Suo, 1992; Beuth, 1992; Ho and Suo, 1993; Chan et al., 1993), as

$$G_t = \frac{1}{a}\int_0^a G_p(a')\mathrm{d}a' \tag{20}$$

and

$$G_t = \frac{1}{2a}\int_H^{H-a} \sigma(a, z)\delta(a, z)\mathrm{d}z \tag{21}$$

Eq. (20) requires the solution of G_p for a plane strain crack of arbitrary length a' ($0 < a' < a$). An evaluation of (21) makes use of the thermal stress distribution $\sigma(a, z)$ on the prospective crack plane prior to cracking and the associated opening profile $\delta(a, z)$ of the crack. Both Eqs. (20) and (21) can be used to calculate G_t. For Eq. (20) the weight function method should be used to determine $G_p(a')$, whereas for Eq. (21) the dislocation method is recommended to determine the crack opening profile $\delta(a, z)$. The results for G_t reported below are calculated from Eq. (21).

For illustration, consider Case I boundary conditions with $Bi = 10$. The normalised energy release rate for steady-state channelling $\bar{G} = G_t/G_0$ is plotted in Fig. 9 as a function of normalised crack length $\bar{a} = a/H$ and normalised time $\bar{t} = \kappa t/H^2$, where $G_0 \equiv \bar{E}\bar{\alpha}^2 H(T_i - T_\infty)^2$. The trends exhibited by G_t for steady-state channelling are similar to those of G_p for plane strain cracking, with the peak value of G_t at any crack depth occurring at $\bar{t} \approx 0.1$ [compare Figs. 6(b) and 9]. The result for G_t as a function of $\bar{a}$ at fixed $\bar{t}$ are qualitatively similar for all three types of boundary condition, and so plots are omitted for the boundary conditions of Cases II and III.

Consider a channelling crack in steady state, with a fixed depth a and a given Biot number Bi. Then G_t attains its peak value $(G_t)_{peak}$ after a time t_{peak}. The associated surface temperature jump $(\Delta T_t)_{peak}$ is determined by equating $(G_t)_{peak}$ with the toughness G_{IC}. The non-dimensional temperature for channelling, $(\Delta \bar{T}_t)_{peak} \equiv (\Delta T_t)_{peak}/\sqrt{G_{IC}/(\bar{E}\bar{\alpha}^2 H)}$, is plotted in Fig. 7(a) against the dimensionless crack size $\bar{a} = a/H$, for $Bi = 10$ and the Case I boundary condition. The results for Cases II and III, with $Bi = 10$, are summarised in Fig. 7(b). We note from Figs. 7(a) and (b) that the critical temperature jump for plane strain

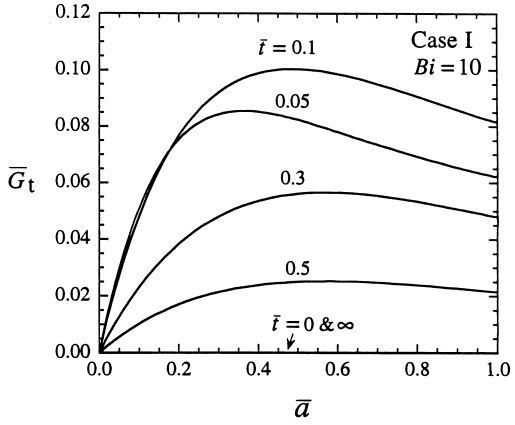

Fig. 9. Energy release rate G_t as a function of crack size and time elapse for steady-state channelling (Case I with $Bi = 10$).

crack growth is less than that for channelling, for small values of crack length [$\bar{a} < 0.5$ in Fig. 7(a), and $\bar{a} < 0.3$ in Fig. 7(b)], whereas channelling is expected to occur in preference to plane strain crack growth at greater crack depths.

The global maximum $(G_t)_{max}$ for any given Biot number is obtained by searching for the maximum value of G_t over all values of crack length and time. As in the case of plane strain cracking, simple curve-fit formulae are obtained for the global maximum energy release rate for steady-state channelling, $(G_t)_{max}$, with

$$(\bar{G}_t)_{max} \equiv \frac{(G_t)_{max}}{G_0} = 0.155\left(1 + \frac{2.2}{Bi}\right)^{-2}, \quad \text{Case I} \tag{22a}$$

$$(\bar{G}_t)_{max} \equiv \frac{(G_t)_{max}}{G_0} = 0.08\left(1 + \frac{2.9}{Bi}\right)^{-2}, \quad \text{Case II and III} \tag{22b}$$

These results can be used together with the fracture criterion $(G_t)_{max} = G_{IC}$ to estimate the maximum temperature jump $(\Delta T_t)_{max}$ that can be applied without channelling. [Again, note that Eq. (22) cannot be applied in the limiting case of $H \to \infty$ at finite h.] The predicted $(\Delta \bar{T}_t)_{max}$, together with the corresponding crack depth $\bar{a}_c = a_c/H$ and elapsed time $\bar{t}_c = \kappa t_c/H^2$, are shown in Fig. 8 as dashed lines and are adequately described by the following curve-fits:

$$(\Delta \bar{T}_t)_{max} \equiv (\Delta T_t)_{max} \frac{\bar{E}\bar{\alpha}\sqrt{H}}{K_{IC}} = 2.54 + \frac{5.4}{Bi} \tag{23a}$$

$$\bar{t}_c \equiv \frac{\kappa t_c}{H^2} = 0.06 + \frac{0.43}{1 + 1.5\ Bi} \tag{23b}$$

$$\bar{a}_c \equiv \frac{a_c}{H} \approx 0.54 \tag{23c}$$

for Case I and

$$(\Delta \bar{T}_t)_{max} \equiv (\Delta T_t)_{max} \frac{\bar{E}\bar{\alpha}\sqrt{H}}{K_{IC}} = 3.53 + \frac{10.0}{Bi} \tag{24a}$$

$$\bar{t}_c \equiv \frac{\kappa t_c}{H^2} = 0.02 + \frac{0.3}{1 + Bi} \tag{24b}$$

$$\bar{a}_c \equiv \frac{a_c}{H} \approx 0.41 \tag{24c}$$

for Cases II and III.

Differentiation of (20) with respect to a gives

$$\frac{dG_t}{da} = \frac{1}{a}(G_p - G_t) \tag{25}$$

and so G_p equals G_t at the local maximum $dG_t/da = 0$, with t held fixed. Consequently, ΔT_t for channelling equals ΔT_p for plane strain cracking at this local maximum. The global maximum for channelling, $G_t = (G_t)_{max}$ occurs at a crack length $\bar{a}_c$ and a time $\bar{t}_c$, and the ΔT_p for plane strain cracking equals $(\Delta T_t)_{max}$ at this time. But, for this value of crack length $\bar{a}_c$, there exists a $(\Delta T_p)_{peak}$ which occurs at some other time and is less than the value ΔT_p. Consequently, the curve of $(\Delta T_p)_{peak}$ versus $\bar{a}$ does not cross the $(\Delta T_t)_{peak}$ versus $\bar{a}$ trajectory at the point where $(\Delta T_t)_{peak}$ attains the turning value $(\Delta T_t)_{max}$.

5. Spalling under thermal shock

Consider again a Mode I edge crack extending normal to the top surface of the plate (Fig. 6(a)). Initially, G_p increases with a and crack growth is dynamically unstable (Fig. 6(b)). However, when the tip of the crack enters a zone of compressive stress in the central portion of the plate, the elastic energy available for continued crack extension decreases — crack extension is now dynamically stable (Fig. 6(b)). The crack may then choose to channel as discussed in Section 4, or to deflect into a spalling path as shown in Fig. 1(c) and analysed below.

5.1. Effect of T-stress on directional stability of crack extension

The path along which a Mode I crack may choose to grow is sensitive to the T-stress. For a Mode I crack extending in an isotropic material, the well-known Williams' asymptotic expansion of in-plane stress components near the crack tip is

$$\sigma_{\alpha\beta} = \frac{K_I}{\sqrt{2\pi r}}\tilde{\sigma}_{\alpha\beta}(\theta) + T^*\delta_{1\alpha}\delta_{1\beta} + O(r^{1/2}), \quad (\alpha, \beta) = 1, 2 \tag{26}$$

where (r, θ) are polar co-ordinates centred at the tip of the crack, $\delta_{\alpha\beta}$ is the Kronecker delta, and T^* is a non-singular stress acting parallel to the crack plane, namely, the T-stress. For anisotropic materials, Eq. (26) can still be used to define the stress intensity factor K_I but the dimensionless functions $\tilde{\sigma}_{\alpha\beta}$ now depend on material properties as well as θ (Sih et al., 1965). Some insight into the value of T^* is obtained by recalling that, for a semi-infinite crack in a full space, the T-stress equals the negative of the normal traction acting on the cracking plane at the location of the crack tip (Lu, 1996). Once the T-stress is known, the directional stability of crack extension is determined: stable if T^* is negative and unstable if T^* is positive (Cotterell and Rice, 1980). Physically, this may be interpreted as follows: when straight-ahead advance of a Mode I crack is perturbed at the crack tip due to micro-heterogeneity such as pores and inclusions, a positive T-stress will render the crack to veer away from the straight path while a negative T-stress will keep the crack in its original straight trajectory. Overall force equilibrium in a

thermally shocked plate dictates that a tensile thermal stress field is *always* accompanied with a compressive thermal stress field; hence, a Mode I crack advancing normal to this stress field has the tendency to kink away from the straight path once its tip enters the compressive zone.

5.2. Initiation and steady-state growth of spalling cracks

Referring to Fig. 10(a), assume that a crack of length a, initially advancing in Mode I in a direction perpendicular to the surface of the plate, branches into two identical cracks parallel to the surface. The doubly deflected crack path is chosen not only for its simplicity, but also because the associated energy release rate and mode mix are, to an excellent approximation, identical to those associated with a singly deflected path (He and Hutchinson, 1994). (The incorrect results for the doubly deflected crack problem contained in the original paper of He and Hutchinson, 1989, are corrected in He et al., 1994.) Although this symmetry is idealised, it is expected to capture the essence of all deflection behaviours. The analysis below will be further restricted to the initiation of kinking ($c/a < 0.1$) and steady-state spalling ($c/a > 1$), with the transient stage ignored. The solutions obtained for steady-state spalling will apply so long as the deflected crack length c is larger than a (Hutchinson and Lu, 1995; Lu, 1996).

5.2.1. Initiation of kinking ($c \ll a$)

Consider a putative kink of length c at right-angles to a parent Mode I crack of length a ($\gg c$). The Mode I and II stress intensity factors at the tip of the kink (K_1, K_2) are related to the stress intensity factors at the tip of the parent crack (K_I, K_{II}) by (Hutchinson and Suo, 1992; He et al., 1994; Lu, 1996)

$$K_1 = 0.398K_I + 1.845T^*\sqrt{c}$$

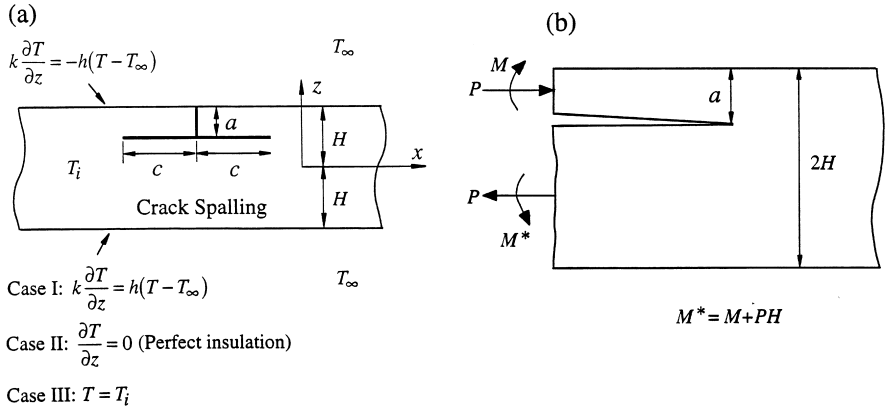

Fig. 10. (a) Model for steady-state spalling, and (b) equivalent edge force and moment.

$$K_2 = 0.323K_I - 0.212T^*\sqrt{c} \tag{27}$$

where the T-stress, T^*, is calculated in Appendix B. The corresponding energy release rate G_s is given by

$$G_s = \frac{1}{\bar{E}}(K_1^2 + K_2^2) \tag{28}$$

Note that the mode mix at the tip of the deflected crack is fairly large, with $\psi \equiv \tan^{-1}(K_2/K_1) = 39.1^\circ$, for the case of a parent crack in pure Mode I. Thus, the kink has a tendency to deviate in path back towards the original direction of growth of the Mode I parent crack. However, if microstructural inhomogeneities are present to keep the kink advancing parallel to the free surface of the plate, a steady-state is achieved for the spalling crack with a new fixed value of crack tip energy release rate and mode mix.

5.2.2. Steady-state spalling ($c \gg a$)

When $c \gg a$, the deflected crack advances in steady-state as shown in Fig. 10(b); the crack is driven by a constant bending moment M and a constant in-plane axial force P per unit depth, related to the thermal stress field by

$$\bar{P} \equiv \frac{P}{\bar{E}\bar{\alpha}H(T_i - T_\infty)} = \int_{1-a/H}^{1} \bar{\sigma}(z/H, t)\mathrm{d}(z/H)$$

$$\bar{M} \equiv \frac{M}{\bar{E}\bar{\alpha}H^2(T_i - T_\infty)} = \int_{1-a/H}^{1} (z/H + a/2H - 1)\bar{\sigma}(z/H, t)\mathrm{d}(z/H) \tag{29}$$

Now, the steady-state energy release rate G_s due to (P, M) and the associated stress intensity factors (K_1, K_2) can be obtained by an energy analysis of the elastic beams far ahead and far behind the crack tip, coupled with arguments based on linearity and dimensionality (Hutchinson and Suo, 1992). The desired results for the steady-state values are

$$\bar{G}_s = \frac{G_s}{G_0} = \frac{1}{2}\left\{ \frac{\bar{P}^2}{A(a/H)} + \frac{\bar{M}^2}{I(a/H)^3} + 2\frac{\bar{P}\bar{M}}{\sqrt{A\bar{I}}(a/H)^2} \sin\ \gamma \right\} \tag{30a}$$

and

$$\frac{K_1}{\bar{E}\bar{\alpha}\sqrt{H}(T_i - T_\infty)} = \frac{\bar{P}}{\sqrt{2\pi A(a/H)}} \cos\ \omega + \frac{\bar{M}}{\sqrt{2\pi I(a/H)^3}} \sin(\omega + \gamma)$$

$$\frac{K_2}{\bar{E}\bar{\alpha}\sqrt{H}(T_i - T_\infty)} = \frac{\bar{P}}{\sqrt{2\pi A(a/H)}} \sin\ \omega - \frac{\bar{M}}{\sqrt{2\pi I(a/H)^3}} \cos(\omega + \gamma) \tag{30b}$$

where

$$\frac{1}{A} = 1 + 4\eta + 6\eta^2 + 3\eta^3, \quad \frac{1}{I} = 12(1+\eta^3), \quad \frac{\sin\ \gamma}{\sqrt{AI}} = 6\eta^2(1+\eta)$$

$$\eta = \frac{a/H}{2 - a/H}, \quad \omega \cong 52.1^\circ - 3^\circ\eta \tag{31}$$

The phase angle ψ of mode mix at the tip of the deflected crack is defined by

$$\psi = \tan^{-1}(K_2/K_1) \tag{32}$$

For Case I temperature boundary condition with $Bi = 10$, the normalised energy release rate $\bar{G}_s$ and the associated phase angle ψ for steady-state spalling are plotted in Figs. 11(a) and (b) as a function of the normalised spalling depth $\bar{a}$, at selected values of normalised time $\bar{t}$. For all values of crack depth $\bar{a}$, $\bar{G}_s$ attains a maximum value at a time $\bar{t} \approx 0.1$ (Fig. 11(a)). The global maximum in $\bar{G}_s$ is attained at $\bar{t} \approx 0.1$ and at $\bar{a} = 1$. A straightforward physical explanation is that at $\bar{t} = \kappa t/H^2 = 0.1$, the two thermal fronts commencing separately from the top and bottom surfaces meet at the mid-point (Lu and Chen, 1999).

The phase angle ψ depends strongly on both $\bar{a}$ and $\bar{t}$, as shown in Fig. 11(b), but a few general remarks can be made. The mid-plane $\bar{a} = 1$ is always a Mode I path, such that $\psi = 0$. For $\bar{t}$ less than about 0.1, there are three possible Mode I paths: the mid-plane and two paths symmetrically disposed to the mid-plane. For $\bar{t}$ greater than about 0.1, a single Mode I path exists along the mid-plane. Recall that a Mode I path is likely to propagate in a stable configuration, without deviation in path, provided $\partial\psi/\partial\bar{a}$ is negative, as discussed by Fleck et al. (1991) and as summarised as follows. Consider a crack located parallel to the path of $\psi = 0$ but placed a small distance $\delta\bar{a}$ below it and assume that $\partial\psi/\partial\bar{a}$ is negative; then, for such a perturbed path, ψ is negative and the crack will tend to kink back towards the Mode I path. Examination of Fig. 11(b) shows that for $\bar{t} \geq 0.1$ the mid-plane is a configurationally stable Mode I path, whereas for $\bar{t} < 0.1$ the mid-plane is configurationally unstable but the adjacent two Mode I paths are stable.

Results for $\bar{G}_s$ and ψ for Cases II and III are presented in Figs. 11(c) and (d). Again, a value $Bi = 10$ is assumed and the dependence of $\bar{G}_s$ and ψ upon the non-dimensional crack depth $\bar{a}$ is plotted for selected values of scale time, $\bar{t}$. At any given time, there exists a single Mode I path, its location shifting gradually with time from near the top surface towards the bottom surface of the plate; the Mode I paths are stable in the sense that $\partial\psi/\partial\bar{a} < 0$.

For a fixed Biot number, the maximum temperature jump to withstand steady-state spalling, $(\Delta T_s)_{peak}$, for any depth $\bar{a}$ of a spalling crack is calculated by equating the maximum value of G_s over all time with the toughness G_{IC}, for that value of $\bar{a}$. The resulting values of $(\Delta\bar{T}_s)_{peak} \equiv (\Delta T_s)_{peak}/\sqrt{G_{IC}/(\bar{E}\bar{\alpha}^2 H)}$ are included in Figs. 7(a) and (b) for the case $Bi = 10$. Let $(G_s)_{max}$ denote the global maximum energy release rate for steady-state spalling at any fixed value of Bi. Simple curve-

fit formulas for $(G_s)_{max}$ are obtained as

$$(\bar{G}_s)_{max} \equiv \frac{(G_s)_{max}}{G_0} = 0.077\left(1+\frac{2.1}{Bi}\right)^{-2}, \quad \text{Case I} \tag{33a}$$

$$(\bar{G}_s)_{max} \equiv \frac{(G_s)_{max}}{G_0} = 0.027\left(1+\frac{2.4}{Bi}\right)^{-2}, \quad \text{Cases II and III} \tag{33b}$$

Note that $(G_s)_{max}$ corresponds to a Mode I path in Case I (Figs. 11(a) and (b)) and a nearly Mode I path in Cases II and III (Figs. 11(c) and (d)). From the fracture criterion $(G_s)_{max} = G_{IC}$, the predicted maximum temperature jump $(\Delta T_s)_{max}$ without spalling is shown in Fig. 8 as dotted lines together with $\bar{a}_c = a_c/H$ and $\bar{t}_c = \kappa t/H^2$. The related curve-fitting formulas are

$$(\Delta\bar{T}_s)_{max} \equiv (\Delta T_s)_{max}\frac{\bar{E}\bar{\alpha}\sqrt{H}}{K_{IC}} = 3.60 + \frac{7.5}{Bi} \tag{34a}$$

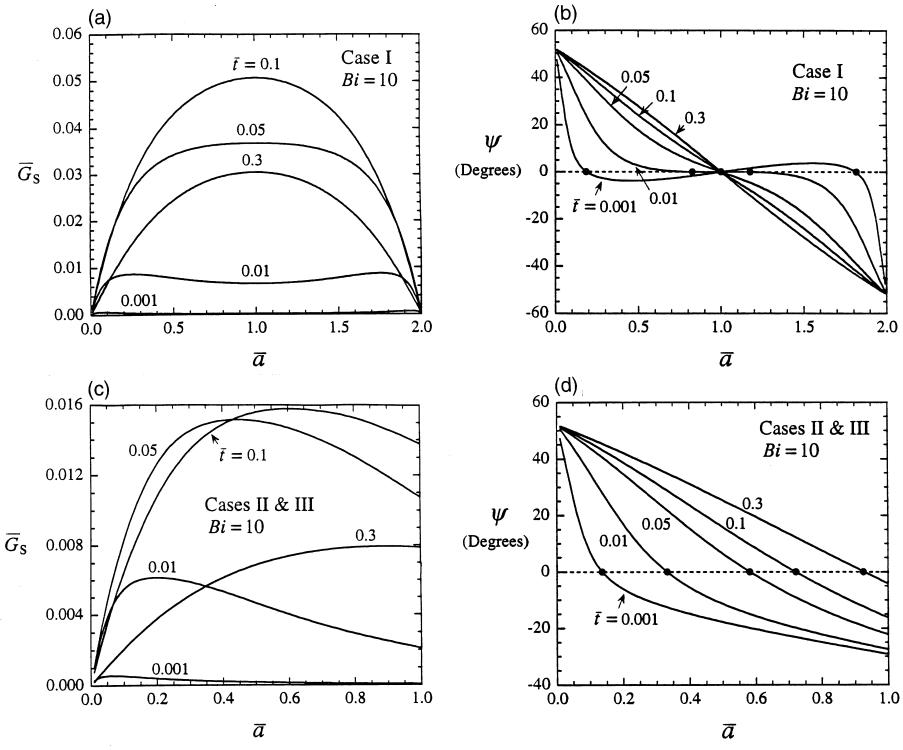

Fig. 11. (a) Energy release rate, (b) phase angle as functions of spalling depth and time for Case I ($Bi = 10$), (c) energy release rate, and (d) phase angle as functions of spalling depth and time for Cases II and III ($Bi = 10$).

$$\bar{t}_c \equiv \frac{\kappa t_c}{H^2} = 0.08 + \frac{0.4}{1 + 1.35\ Bi} \tag{34b}$$

$$\bar{a}_c \equiv \frac{a_c}{H} = 1.0 \tag{34c}$$

for Case I and

$$(\Delta \bar{T}_s)_{max} \equiv (\Delta T_s)_{max} \frac{\bar{E}\bar{\alpha}\sqrt{H}}{K_{IC}} = 6.08 + \frac{14.8}{Bi} \tag{35a}$$

$$\bar{t}_c \equiv \frac{\kappa t_c}{H^2} = 0.04 + \frac{0.35}{1 + Bi} \tag{35b}$$

$$\bar{a}_c \equiv \frac{a_c}{H} = 0.44 + \frac{0.35}{1 + 0.25\ Bi} \tag{35c}$$

for Cases II and III. It is clear from Fig. 8(a) that the maximum temperature that can be applied without steady state spalling exceeds that for plane strain cracking and channelling, for all three cases of thermal boundary condition, and for all values of Biot number. Finally, we note in passing that Eqs. (33)–(35) do not apply in the case of $H \to \infty$ at finite h.

6. Solutions in the short crack limit

At sufficiently short times after thermal shock loading of a plate, the temperature and stress distributions decay rapidly a small distance from the surface of the plate, and the plate behaves as a semi-infinite solid. In this section, we study the response of a plane strain crack, a channelling crack and a spalling crack within a semi-infinite solid when its surface is subjected to a thermal shock. These asymptotic solutions are good approximations to the finite plate case provided the crack length a is small compared to the specimen thickness $2H$, and provided the time t is sufficiently short. The range of validity of these short crack solutions will be quantified for various values of h. The limiting case $h \to \infty$ for plane strain cracking of an infinite solid has already been solved by Hutchinson and Suo (1992); no analytical solutions appear to exist for crack channelling and spalling within an infinite solid.

6.1. Plane strain cracking

In the limit $a/H \to 0$, the plane strain cracking problem is reduced to that of an edge crack of length a in a semi-infinite solid subjected to a cold shock on the surface [see Fig. 12(a), where $z = 0$ is now placed on the surface of the solid]. Then, the boundary condition on the surface becomes

$$k\frac{\partial T}{\partial z} = -h(T - T_\infty) \quad \text{at } z = 0 \tag{36}$$

and the resulting temperature distribution in the block is given by (Carslaw and Jaeger, 1959)

$$\begin{aligned}\bar{T}\left(\frac{z}{a}, \frac{\sqrt{\kappa t}}{a}, Bi^*\right) &\equiv \frac{T - T_i}{T_i - T_\infty} = -1 + \operatorname{erf}\left\{\frac{z}{a}\frac{a}{2\sqrt{\kappa t}}\right\} \\ &+ \exp\left\{Bi^*\frac{z}{a} + \left(Bi^*\frac{\sqrt{\kappa t}}{a}\right)^2\right\}\operatorname{erfc}\left(\frac{z}{a}\frac{a}{2\sqrt{\kappa t}} + Bi^*\frac{\sqrt{\kappa t}}{a}\right)\end{aligned} \tag{37}$$

where $\operatorname{erf}(x = (2/\sqrt{\pi})\int_0^x \exp(-\zeta^2)\mathrm{d}\zeta$ is the error function, $\operatorname{erfc}(x) = 1 - \operatorname{erf} x$, and $Bi^* = ha/k$ is a new Biot number based on the crack length a (compare with $Bi = hH/k$ for the finite plate). The thermal stress field due to the temperature transients is (Hutchinson and Suo, 1992)

$$\bar{\sigma}\left(\frac{z}{a}, \frac{\sqrt{\kappa t}}{a}, Bi^*\right) \equiv \frac{\sigma_{xx}(z, t)}{\bar{E}\bar{\alpha}(T_i - T_\infty)} = -\bar{T}\left(\frac{z}{a}, \frac{\sqrt{\kappa t}}{a}, Bi^*\right) \tag{38}$$

and the normalised stress intensity factor at the tip of the plane strain edge crack of length a is (Tada et al., 1985)

$$\begin{aligned}\hat{K}_I\left(\frac{\sqrt{\kappa t}}{a}, Bi^*\right) &\equiv \frac{K_I}{\bar{E}\bar{\alpha}(T_i - T_\infty)\sqrt{\pi a}} \\ &= -\frac{2}{\pi}\int_0^1 \frac{\bar{T}}{\sqrt{1 - (z/a)^2}}\{1.3 - 0.3(z/a)^{5/4}\}\mathrm{d}\left(\frac{z}{a}\right)\end{aligned} \tag{39}$$

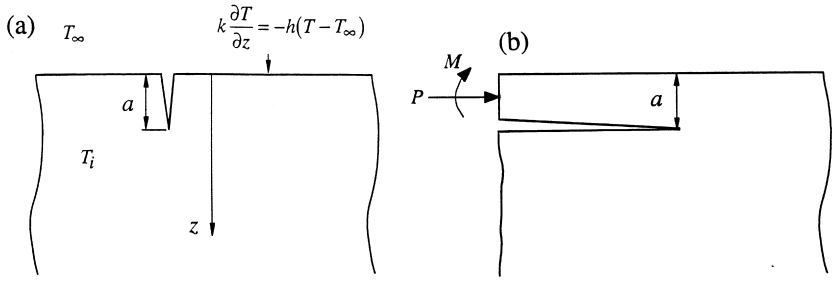

Fig. 12. (a) An edge crack in a half space under cold shock, and (b) steady-state spalling in a half space.

Consequently, the normalised energy release rate for plane strain cracking is

$$\hat{G}_{\mathrm{p}}\left(\frac{\sqrt{\kappa t}}{a},\, Bi^{*}\right) \equiv \frac{G_{\mathrm{p}}}{\bar{E}\bar{\alpha}^{2}(T_{\mathrm{i}}-T_{\infty})^{2}a} = \pi(\hat{K}_{\mathrm{I}})^{2} \tag{40}$$

It is instructive — and also practically relevant — to determine the ranges over which the solution (37)–(40) is valid for an edge crack of the same length extending in a plate of finite thickness $2H$. For the Case I cold shock, the normalised stress intensity factor for an edge crack in a plate of thickness $2H$ is plotted in Fig. 13(a) as a function of normalised time $\kappa t/a^{2}$, at $Bi^{*}=ha/k = 1$. Results are plotted for selected ratios of crack length a to plate semi-thickness H, including the limiting case of an edge crack in a half-space $a/H = 0$. The solutions for an edge crack with thermal boundary conditions given by Case II and III, and for channelling cracks with all three types of thermal boundary condition, show similar trends to those shown in Fig. 13(a). For any given a/H ratio and Biot number Bi^{*}, the stress intensity factor at the tip of an edge crack in a half-space is nearly identical to that at the tip of an edge crack in a finite plate, provided the normalised time $\kappa t/a^{2}$ is smaller than a critical value $\kappa t^{*}/a^{2}$. In general, the value of this critical time increases with decreasing a/H and with decreasing Bi^{*}. For definiteness, let $\kappa t^{*}/a^{2}$ denote the time interval over which the asymptotic solution for an edge crack of length a in a half-space is within 10% of the solution for an edge crack, of length a, in a plate of given thickness $2H$, and subjected to the same cold shock. The interval $\kappa t^{*}/a^{2}$ is plotted in Fig. 13(b) as a function of a/H

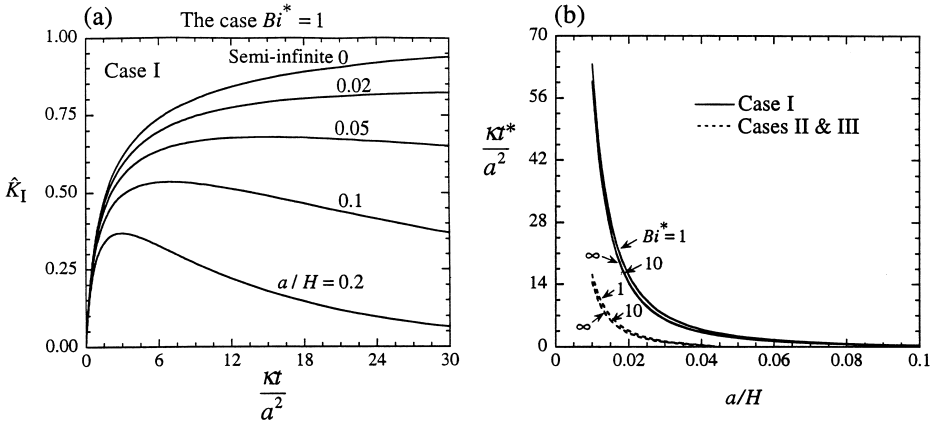

Fig. 13. (a) Stress intensity factor as a function of dimensionless time $\kappa t/a^{2}$ for selected value of a/H, subjected to Case I cold shock with $Bi^{*}=1$, and (b) range of validity for the short crack solutions.

and Bi^* for all three cases of thermal boundary condition. Observe that $\kappa t^*/a^2$ depends strongly on a/H, and only weakly on Bi^*.

6.2. Steady-state channelling

For steady-state channelling of an edge crack in a half-space the normalised energy release rate is related to that for plane strain cracking by

$$\hat{G}_t\left(\frac{\sqrt{\kappa t}}{a}, Bi^*\right) \equiv \frac{G_t}{\bar{E}\bar{\alpha}^2(T_i - T_\infty)^2 a} = \frac{1}{a}\int_0^a \hat{G}_p(a')\,da' \tag{41}$$

Fig. 14(a) plots $\hat{G}_p$ and $\hat{G}_t$ as functions of dimensionless time $\kappa t/a^2$ and Biot number $Bi^* = ha/k$. Note that both $\hat{G}_p$ and $\hat{G}_t$ reach their global maximum values $\hat{G}_p^\infty = 2\hat{G}_t^\infty = 3.96$ in the limit $\kappa t/a^2 \to \infty$; this corresponds to a state of uniform thermal stress $\bar{\sigma}_{xx} = 1$ over the full depth of the crack, with $\hat{K}_I^\infty = 1.1215$. These limiting values are independent of the surface heat transfer coefficient h (or Biot number Bi^*). On applying the toughness-based fracture criterion $G_p = G_{IC}$ and $G_t = G_{IC}$, the maximum surface temperature jump which the half-space can sustain is $(\Delta T)_{max} = 0.5\sqrt{G_{IC}/\bar{E}\bar{\alpha}^2 a}$ for plane strain cracking, and $(\Delta T)_{max} = 0.71\sqrt{G_{IC}/\bar{E}\bar{\alpha}^2 a}$ for channelling.

The half-space solution give in Fig. 14(a) is valid for a finite plate of sufficient thickness $2H$ in relation to the crack length a. Since the channelling solution is derived directly from the plane strain cracking solution via (41), the minimum

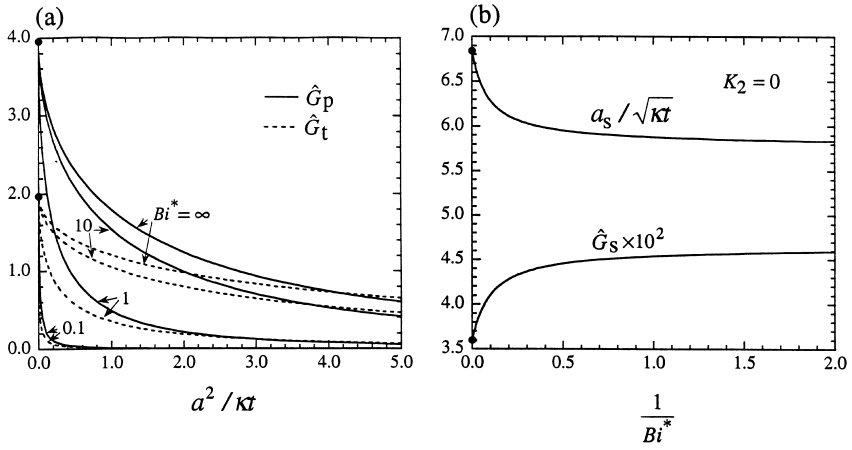

Fig. 14. (a) Energy release rate as a function of dimensionless time $\kappa t/a^2$ for selected values of Biot number Bi^* for plane strain cracking G_p and channelling G_t, and (b) energy release rate along the Mode I spalling path and the corresponding spalling depth as functions of Bi^*.

thickness $2H$ for which the channelling solution in Fig. 14(a) is accurate can be read from Fig. 13(b), for given values of (a, t, Bi^*).

6.3. Steady-state spalling

Consider the case of a spalling crack parallel to the free surface of a half-space, after a cold shock has been imposed with boundary condition (36). The physical problem is illustrated in Fig. 12(b). Far ahead of the crack tip, the stress and temperature distributions are given by (37) and (38). Hutchinson and Suo (1992) have already considered this problem for the case of ideal heat transfer, $h=\infty$, and their findings are summarised here before extending their results to include the case when h is finite. For the case $h=\infty$, a Mode I crack path exists parallel to the free surface, at any value of time, t. As t increases, both the energy release rate and the depth of the Mode I spalling crack increase. Hutchinson and Suo (1992) argue that the spalling depth and the associated time to spalling are set by applying the fracture criterion $G_s=G_{IC}$.

Now consider the case of steady-state spalling, with a finite value of heat transfer h at the surface of the half-space. The equivalent edge force and moment indicated in Fig. 12(b) are

$$\hat{P} \equiv \frac{P}{\bar{E}\bar{\alpha}a(T_i - T_\infty)} = \int_0^1 \bar{\sigma}\left(\frac{z}{a}, \frac{\sqrt{\kappa t}}{a}, Bi^*\right)\mathrm{d}\left(\frac{z}{a}\right)$$

$$\hat{M} \equiv \frac{M}{\bar{E}\bar{\alpha}a^2(T_i - T_\infty)} = \int_0^1 \bar{\sigma}\left(\frac{z}{a}, \frac{\sqrt{\kappa t}}{a}, Bi^*\right)\left(\frac{1}{2} - \frac{z}{a}\right)\mathrm{d}\left(\frac{z}{a}\right) \tag{42}$$

and the corresponding energy release rate and stress intensity factors are given by

$$\hat{G}_s = \frac{G_s}{\bar{E}\bar{\alpha}^2 a(T_i - T_\infty)^2} = \frac{1}{2}\{\hat{P}^2 + 12\hat{M}^2\} \tag{43}$$

and

$$\frac{K_1}{\bar{E}\bar{\alpha}\sqrt{a}(T_i - T_\infty)} = \frac{\hat{P}}{\sqrt{2\pi}}\cos\ \omega + \frac{\hat{M}}{\sqrt{\pi/6}}\sin\ \omega$$

$$\frac{K_2}{\bar{E}\bar{\alpha}\sqrt{a}(T_i - T_\infty)} = \frac{\hat{P}}{\sqrt{2\pi}}\sin\ \omega - \frac{\hat{M}}{\sqrt{\pi/6}}\cos\ \omega \tag{44}$$

where $\omega = 52.07^\circ$. Extensive calculations have been carried out to determine $\hat{G}_s$ and the phase angle $\psi = \tan^{-1}(K_2/K_1)$ as functions of $\kappa t/a^2$ and Bi^*. It is found that both $\hat{G}_s$ and ψ increase with increasing time t and with increasing heat transfer coefficient h, although the dependence of ψ on h is weak; in the limit $\kappa t/a^2 \to \infty$, $\hat{G}_s \to 0.5$ and $\psi \to 52.07^\circ$. In Fig. 14(b), the values of $\hat{G}_s$ and $a_s/\sqrt{\kappa t}$

corresponding to the Mode I spalling path ($K_2 = 0$) are plotted as functions of Bi^*. Note that $a_s/\sqrt{\kappa t}$ is relatively insensitive to the Biot number Bi^*, especially when $Bi^* < 1$. In the limit $Bi^* \to \infty$, the results reduce to those obtained by Hutchinson and Suo (1992), i.e., $G_s = 0.036 a_s \bar{E}\bar{\alpha}^2 \Delta T^2$ (or, equivalently, $K_1 = 0.190 \bar{E}\bar{\alpha}\Delta T\sqrt{a_s}$) and $a_s = 6.82\sqrt{\kappa t}$. For illustration, consider the same choice of glass as made by Hutchinson and Suo (1992), with $K_{IC} = 0.7$ MPa$\sqrt{\text{m}}$, $\bar{E}\bar{\alpha}\Delta T = 100$ MPa and $\kappa = 0.7 \times 10^{-6}$ m^2/s. The predicted spalling depth for $Bi^* = \infty$ is $a_s = 1.4$ mm, associated with a time elapse of $t = 0.06$ s. In view of Fig. 14(b), this time will increase slightly when the idealised boundary condition $Bi^* = \infty$ is replaced by one having a finite Biot number.

The spalling crack solution given in Fig. 14(b) for a semi-infinite solid is best understood as follows. For assumed values of crack depth a, heat transfer coefficient h and material toughness G_{IC}, the value of Biot number Bi^* is calculated, and the corresponding values of $a_s/\sqrt{\kappa t}$ and $\hat{G}_s$ are read from the figure. On assuming that cracking occurs when $G_s = G_{IC}$, the required temperature jump for spalling is deduced directly from the definition $\hat{G}_s \equiv [G_s/\bar{E}\bar{\alpha}^2 a(T_i - T_\infty)^2]$, and the time for spalling is deduced from the value of $a_s/\sqrt{\kappa t}$. We expect the asymptotic solution for spalling of the semi-infinite solid to adequately represent the solution for a finite plate provided the spalling time is less than t^*, as plotted in Fig. 13(b).

7. Merit indices for thermal shock

The results presented above can be analysed to obtain appropriate material indices that govern thermal shock fracture in the full range of Biot numbers. Two failure criteria may be used, one based on strength and the other based on fracture toughness. The stress-based fracture criterion assumes that $\sigma_{max}(H, t)$ attains the fracture strength of the solid σ_f, whereas the toughness-based fracture criterion assumes that $K_{max}(a_c, t_c)$ attains the fracture toughness of the solid K_{IC}.

In the case of ideal heat transfer ($Bi = \infty$), the maximum surface temperature jump ΔT that can be tolerated without causing strength-controlled failure follows directly from (9a) and (b) as

$$\Delta T \approx \frac{\sigma_f}{E\alpha} \tag{45}$$

which is valid for Cases I to III. Here, the distinctions between E and $\bar{E}$, and between α and $\bar{\alpha}$ have been dropped, as only those properties of primary significance are considered for selecting materials. In the limit of small Biot number ($Bi < 1$), ΔT is again obtained from Eqs. (9a) and (b) as

$$\Delta T = A_1 \frac{\sigma_f}{E\alpha} \frac{k}{hH} \tag{46}$$

where $A \approx 3.2$ for Case I and $A_1 \approx 5.5$ for Cases II and III. With relations (45)

and (46) in hand, the optimal materials to withstand strength-dominated fracture by thermal shock can be selected from a plot with $\sigma_f/E\alpha$ and $k\sigma_f/E\alpha$ as axes. Lu and Fleck (1998) have displayed such a plot for a wide range of engineering ceramics.

A similar approach can be adopted for materials selection against crack propagation under a cold shock. We assume that the maximum surface temperature jump sustainable by a cracked plate of thickness $2H$ is associated with plane strain cracking; a worst flaw is considered, with the crack depth equal to the critical value a_c to give the highest energy release rate. Then the temperature jump ΔT equals $(\Delta T_p)_{max}$, as specified in Eqs. (18a). Since $(\Delta T_p)_{max}$ is a function of the Biot number Bi, the worst case is taken with $Bi \to \infty$ and ΔT given by

$$\Delta T = A_2 \frac{K_{IC}}{E\alpha\sqrt{H}} \tag{47}$$

Here, $A_2 \approx 2.3$ for the Case I thermal boundary condition, and $A_2 \approx 3.2$ for Cases II and III. Similarly, in the limit of small Biot number ($Bi < 1$), the thermal shock fracture resistance becomes

$$\Delta T = A_3 \frac{K_{IC}}{E\alpha\sqrt{H}} \frac{k}{hH} \tag{48}$$

where $A_3 \approx 5.1$ for the Case I boundary condition and $A_3 \approx 9.2$ for Cases II and III. The optimal materials to withstand toughness-controlled fracture by thermal shock can be selected from a plot with $K_{IC}/E\alpha$ and $kK_{IC}/E\alpha$ as axes. Lu and Fleck (1998) have already displayed a large number of engineering ceramics on a materials selection map of this type.

Acknowledgements

The authors are grateful for the financial support from the ONR Grant 0014-91-J-1916.

Appendix A. Temperature and stress fields (Cases II and III)

For a plate of finite thickness subjected to Case II boundary condition, the non-dimensional temperature field is given by

$$\bar{T}(z, t) = -1 + 2\sum_{n=1}^{\infty} \frac{\sin\beta_n \cos\{\beta_n(z+H)/2H\}}{\beta_n + \sin\beta_n \cos\beta_n} \exp\left(-\frac{\beta_n^2}{4}\frac{\kappa t}{H^2}\right) \tag{A1}$$

where β_n are the positive roots of $\beta \tan\beta = 2\,Bi$. The corresponding stress field is

$$\bar{\sigma}(z,\,t) = -2\sum_{n=1}^{\infty}\frac{\sin\ \beta_n}{\beta_n+\sin\ \beta_n\ \cos\ \beta_n}\left\{\cos\left(\beta_n\frac{z+H}{2H}\right)-\frac{\sin\ \beta_n}{\beta_n}\right\} \times\exp\left(-\frac{\beta_n^2}{4}\frac{\kappa t}{H^2}\right)+\frac{6z}{H}\sum_{n=1}^{\infty}\frac{\sin\ \beta_n}{\beta_n+\sin\ \beta_n\ \cos\ \beta_n}\left\{\frac{2(\cos\ \beta_n-1)}{\beta_n^2} +\frac{\sin^2\beta_n}{\beta_n}\right\}\exp\left(-\frac{\beta_n^2}{4}\frac{\kappa t}{H^2}\right) \tag{A2}$$

Similarly, for a plate under Case III thermal loading, the evolution of temperature and stress is given by

$$\bar{T}(z,\,t) = -\frac{Bi}{1+Bi}\ \frac{z+H}{2H}-2\sum_{n=1}^{\infty}\frac{\cos\ \beta_n\ \sin\{\beta_n(z+H)/2H\}}{\beta_n-\sin\ \beta_n\ \cos\ \beta_n}\exp\left(-\frac{\beta_n^2}{4}\frac{\kappa t}{H^2}\right) \tag{A3}$$

$$\bar{\sigma}(z,\,t) =2\sum_{n=1}^{\infty}\frac{\cos\ \beta_n}{\beta_n-\sin\ \beta_n\ \cos\ \beta_n}\left\{\sin\left(\beta_n\frac{z+H}{2H}\right)+\frac{(\cos\ \beta_n-1)}{\beta_n}\right\} \times\exp\left(-\frac{\beta_n^2}{4}\frac{\kappa t}{H^2}\right)-\frac{6z}{H}\sum_{n=1}^{\infty}\frac{\cos\ \beta_n}{\beta_n-\sin\ \beta_n\ \cos\ \beta_n} \times\left\{\frac{2(\sin\ \beta_n-\beta_n\ \cos\ \beta_n)}{\beta_n^2}+\frac{(\cos\ \beta_n-1)}{\beta_n}\right\}\exp\left(-\frac{\beta_n^2}{4}\frac{\kappa t}{H^2}\right) \tag{A4}$$

where β_n are the positive roots of $\beta\cot\beta=-2\ Bi$.

Appendix. Calculation of T-stress

For a finite plate of thickness $2H$ (Fig. 6(a)), let $T_G(z,\,a)$ be the Green's function for the T-stress T^* associated with a single edge crack of length a such that

$$T^*(a,\,t) = \int_{H-a}^{H} T_G(z,\,a)\sigma(z,\,t)\mathrm{d}z \tag{B1}$$

where $\sigma(z,\,t)\equiv\sigma_{xx}(z,\,t)$ is the thermal stress parallel to the plate surface. Fett (1997) obtained an approximate expression for $T_G(z,\,a)$ by using the boundary-collocation method. Substitution of his results into (B1) leads to

$$T^*(a,\,t) = -\sigma(a,\,t)+\int_{H-a}^{H} T_G^*(z,\,a)\sigma(z,\,t)\mathrm{d}z \tag{B2}$$

where

$$T^*_G(z, a) = (1 - 4A^*_0)\frac{2z}{a^2} \tag{B3}$$

With $\phi = a/2H$, the dimensionless coefficient A^*_0 is given by

$$A^*_0 = \frac{0.13149 - 0.6203\phi + 0.88823\phi^2 - 0.65955\phi^3 + 0.2139\phi^4}{(1-\phi)^2} \tag{B4}$$

References

Beuth, J.R., 1992. Cracking of thin bonded films in residual tension. International Journal of Solids and Structures 29, 1657–1675.

Carslaw, H.S., Jaeger, J.C., 1959. Conduction of Heat in Solids. Oxford University Press, Oxford.

Chan, K.S., He, M.Y., Hutchinson, J.W., 1993. Cracking and stress redistribution in ceramic layered composites. Material Science Engineering A167, 57–64.

Civelek, M.B., 1985. Stress intensity factors of a system of cracks in an infinite strip. In: Kanninen, M.F., Hopper, A.T. (Eds.), Fracture Mechanics: Sixteenth Symposium, ASTM STP 868, American Society for Testing and Materials, Philadelphia, pp. 7–26.

Cotterell, B., Rice, J.R., 1980. Slightly curved or kinked cracks. International Journal of Fracture 16, 155–169.

Erdogan, F., Gupta, G.D., Cook, T.S., 1973. Numerical solution of singular integral equations. In: Sih, G.C. (Ed.), Methods of Analysis and Solutions of Crack Problems. Noordhoff, Leyden, The Netherlands, pp. 368–425.

Fett, T., 1997. A Green's function for *T*-stresses in an edge-cracked rectangular plate. Engineering Fracture Mechanics 57, 365–373.

Fleck, N.A., Hutchinson, J.W., Suo, Z., 1991. Crack path selection in a brittle adhesive layer. International Journal of Solids and Structures 27, 1683–1703.

Hasselman, D.P.H., 1969. Unified theory of thermal shock fracture initiation and crack propagation in brittle ceramics. Journal of the American Ceramic Society 52, 600–604.

He, M.Y., Hutchinson, J.W., 1989. Crack deflection at an interface between dissimilar elastic materials. International Journal of Solids and Structures 25, 1053–1068.

He, M.Y., Evans, A.G., Hutchinson, J.W., 1994. Crack deflection at an interface between dissimilar elastic materials: role of residual stresses. International Journal of Solids and Structures 31, 3443–3455.

Ho, S., Suo, Z., 1993. Tunnelling cracks in constrained layers. ASME Journal of Applied Mechanics 60, 890–894.

Hutchinson, J.W., Lu, T.J., 1995. Delamination due to high through-thickness temperature gradients. Journal of Engineering Material and Technology 117, 386–390.

Hutchinson, J.W., Suo, Z., 1992. Mixed mode cracking in layered materials. Advances in Applied Mechanics 29, 63–191.

Jin, Z.-H., Mai, Y.-W., 1995. Effects of damage on thermal-shock behaviour of ceramics. Journal of the American Ceramic Society 78, 1873–1881.

Lu, T.J., 1996. Crack branching in all-oxide ceramic composites. Journal of American Ceramic Society 79, 266–274.

Lu, T.J., Chen, C., 1999. Thermal transport and fire retardance properties of cellular aluminium alloys. Acta Materialia 47, 1469–1485.

Lu, T.J., Fleck, N.A., 1998. The thermal shock resistance of solids. Acta materialia 46, 4755–4768.

Manson, S.S., 1966. Thermal Stress and Low-Cycle Fatigue. McGraw-Hill, New York.

Nied, H.F., 1983. Thermal shock fracture in an edge-cracked plate. Journal of Thermal Stresses 6, 217–229.

Rizk, A.E.-F.A., Radwan, S.F., 1993. Fracture of a plate under transient thermal stresses. Journal of Thermal Stresses 16, 79–102.

Sih, C.G., Paris, P.C., Irwin, G.R., 1965. On cracks in rectilinearly anisotropic bodies. International Journal of Fracture 1, 189–203.

Tada, H., Paris, P.C., Irwin, G.R., 1985. Stress Analysis of Cracks Handbook. Del Research, St Louis, MI.